Experimental evidence of the superfocusing effect for axially channeled MeV protons

M. Motapothula,[1,*] S. Petrović,[2] N. Nešković,[2] and M. B. H. Breese[1,†]

[1]*Center for Ion Beam Applications, Physics Department, National University of Singapore, Lower Kent Ridge Road, Singapore 117542*

[2]*Laboratory of Physics, Vinča Institute of Nuclear Sciences, University of Belgrade, P.O. Box 522, 11001 Belgrade, Serbia*

(Received 16 February 2016; published 11 August 2016; corrected 22 August 2016)

Sub-Ångström focusing of megaelectronvolt (MeV) ions within axial channels was predicted over 10 years ago, but evidence proved elusive. We present experimental angular distributions of axially channeled MeV protons in a 55-nm-thick (001) silicon membrane through which multiple scattering is negligible. Fine angular structure is in excellent agreement with Monte Carlo simulations based on three interaction potentials, providing indirect evidence of the existence of the superfocusing effect with flux enhancement of around 800 within a focused beam width of ∼20 pm.

DOI: 10.1103/PhysRevB.94.075415

When a parallel beam of ions enters a crystal at axial alignment, the ions oscillate in channels between atomic strings, giving rise to the channeling effect [1]. This effect has been rigorously pursued theoretically and experimentally for more than 50 years over a wide energy spectrum, from kiloelectronvolt (keV) energies for ion implantation to megaelectronvolt (MeV) energies for ion beam analysis to teraelectronvolt (TeV) energies for proton beam extraction/collision experiments [1–4]. The channeled beam is first focused onto a small cross-sectional area within each channel at a depth corresponding to one quarter of the oscillation wavelength. Demkov and Meyer [5] calculated that a 1 MeV proton beam that was incident on a (001) silicon crystal surface was focused to a width smaller than twice the lattice thermal vibrational amplitude, $\rho_{\text{th}} = 7.8$ pm, with ∼30% of ions focused into a peak area of radius ρ_{th}. They named this the effect the superfocusing effect, with a calculated flux enhancement within the focused beam of ∼1000 passing through an area $\pi\rho_{\text{th}}^2$. This study reopened the theory of flux-peaking effect [6], which occurs when statistical equilibrium in the transverse plane is established, within the framework of applying it for subatomic microscopy where a dopant atom in such a focusing area may undergo a nuclear reaction or X-ray emission. The superfocusing effect compares to the flux-peaking effect, where a maximum flux enhancement of two- to threefold was measured in statistical equilibrium [7]. The superfocusing effect was further investigated in simulations by Nešković *et al.* [8] and Petrović *et al.* [9] for 2 and 68 MeV protons channeled in a (001) silicon crystal at depths of around 83 nm and 482 nm, respectively. Their approach was more realistic than that in Ref. [5], but the results were similar.

None of the predictions in theoretical modeling and simulations of the superfocusing effect related to small proton beam widths and strong flux enhancements has been experimentally verified. Such verification was the motivation of this study, which compares experimental and simulated angular distributions of protons with energies between 2 and 0.65 MeV transmitted through a 55-nm-thick (001) silicon crystal.

We used the FLUX three-dimensional Monte Carlo simulation code [10,11] into which different ion-atom interaction potential models can be inserted. This code uses the binary collision approximation and takes into account lattice thermal vibration and collisions of ions with crystal electrons, allowing realistic modeling of the scattering of an ion beam in its passage through a thin crystal. The choice of the potential plays a crucial role in modeling the ion-crystal interaction [12]; this is particularly true in very thin crystals, where the resulting spatial and angular distributions are dominated by the potential and are only weakly influenced by the multiple scattering effect, unlike in thicker crystals. There are three potential models commonly used in channeling studies, namely, the Ziegler-Biersack-Littmark (ZBL) and Molière models, which do not consider the electronic shell structure of atoms, and the Hartree-Fock (HF) model, which is mostly based on solid state electron densities [10]. Discrepancies between experimental data and different models have been reported in the literature for backscattering measurements in the channeling mode. In Ref. [13], the ZBL potential was used, and in Ref. [14], the Molière potential was chosen, whereas in Ref. [15], it was emphasized that the HF model should be the correct one. A modified form of the Molière potential is called the Rainbow-Molière potential. We performed FLUX simulations with all three potential models in order to best interpret our experimental data within the context of the superfocusing effect. The Rainbow-Molière potential provides the best agreement with our experimental results [16], and here we base our results on this model.

Figure 1(a) shows the FLUX simulated trajectories of protons incident on a 55-nm-thick (001) silicon crystal for entrance proton positions of ±0.6 Å along the direction toward the atomic strings and proton energies of 2.0, 1.0, 0.86, and 0.5 MeV, assuming the Rainbow-Molière potential. For a proton energy of 860 keV, the trajectories are focused at the crystal exit face. In the corresponding simulated exit spatial distributions of protons uniformly incident across the (001) channel, the proton beam is focused at the channel center with a full-width-at-half-maximum (FWHM) of ∼21 pm [Fig. 1(b)]. Those protons incident around the channel center determine this narrow beam width. Those protons incident closer to the atomic strings have a more complex motion, providing the low background intensity within the exit spatial distribution.

*Corresponding author: malli@nus.edu.sg

†Corresponding author: phymbhb@nus.edu.sg

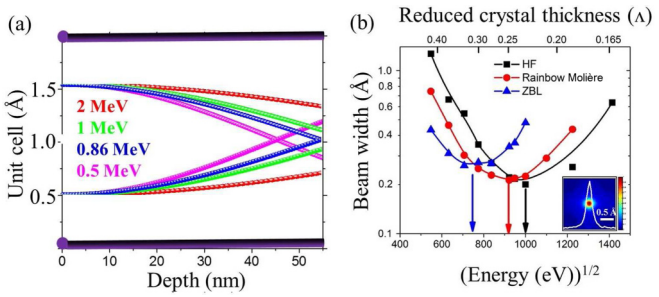

FIG. 1. (a) Schematic showing different proton beam energies passing along the [001] axial channels of a 55-nm-thick silicon membrane. Viewed perpendicular to the (011) direction, coordinates have the same entrance position located midway between atomic strings. (b) Simulated FWHM of superfocused proton distribution versus ion energy for the ZBL, HF, and Rainbow-Molière potentials at the exit face of a 55-nm-thick [001] Si layer. Inset shows the overlap of simulated exit coordinate distribution and line profile under the superfocused condition for the Rainbow-Molière potential.

Figure 1(b) also shows the FWHM of the focused beam peak versus proton energy for the ZBL, Rainbow-Molière, and HF potentials. Using the definition introduced by Krause *et al.* [17,18] for the axial oscillation wavelength, where the reduced crystal thickness, Λ, is equal to $f_h L/v_0$, where L is the crystal thickness, v_0 is the initial proton velocity, and f_h is the frequency of proton motion close to the channel axis, the top axis of Fig. 1(b) shows the values of Λ corresponding to the beam energies based on the Rainbow-Molière potential, where the focused beam width is minimum at 860 keV, corresponding to $\Lambda = 0.25$. It is noteworthy that the beam width changes slowly with Λ; i.e., a superfocused beam is achieved over a relatively wide range of beam energies and so in principle is rather easy to create. Simulations of the beam width versus proton energy for the other potentials give similar behavior, with small differences in the minimum focused beam width (∼20 pm for the HF potential and ∼27 pm for the ZBL potential) and somewhat larger differences in the energy at which this is achieved (∼1000 keV for the HF potential and ∼555 keV for the ZBL potential).

Since all three potentials provide similar results for the focused proton beam width, though with a significantly different energy dependence, we consider that the choice of the potential does not influence the main two outcomes of this study. The first outcome provides an indirect link between experimental observations of fine angular structure and the superfocusing effect. The second outcome confirms good agreement between the experimental and simulated angular patterns using the Rainbow-Molière potential close to $\Lambda = 0.25$, supporting the assumption that the spatial focusing effect in the same simulation correctly results in a focused proton beam width of around 20 pm and a flux enhancement within the focused beam of several hundred fold.

The angular deflection experienced by axially channeled ions when they first interact with the crystal depends on their entrance location across the potential distribution at the channel surface [19,20]. In thick layers, any fine structure within the transmitted angular distribution is blurred by multiple scattering, whereas within a thin crystal layer, the angular distribution is complex and has been predicted to contain fine angular structure in the form of resolved dots [17,18]. This fine angular structure was glimpsed by Krause *et al.* in experiments using 2–9 MeV protons and 6–30 MeV carbon ions transmitted through (001) silicon crystals [17,18]. Those measurements provided an intriguing glimpse of the angular distribution of ions within an axial channel under highly nonequilibrium conditions. The origin of this fine angular structure was later elucidated using the theory of crystal rainbows [18,21,22], which was formulated as a generalized theory of rainbows in ion channeling, predicting the form of these angular distributions versus crystal thickness.

The measurements of Krause *et al.* [17,18] were limited first by the difficulty in fabricating thin silicon membranes that remained fully crystalline, and second by the use of a position-sensitive detector with an inherently slow count rate of ∼1000 ions per second, which limited the ability to resolve faint dots owing to low counting statistics. A new silicon membrane fabrication process was recently developed that enables production of ultrathin (001) silicon layers of 55 nm thickness with a very low surface roughness of 0.4 nm [23]. These membranes allow the study of early stages of ion trajectories along axial channels with very high angular resolution owing to very low multiple scattering, so that any fine structure can be revealed. Channeling patterns are recorded by photographing a highly sensitive yttrium-aluminum-garnet (YAG) scintillator screen 50 cm downstream of the membrane with a camera exposure time of the order of 1 second [22]. This simple system allows rapid recording of intense and faint angular structures simply by varying the exposure. These ultrathin membranes and recording system formed the basis of our recent high-resolution channeling measurements [24–26] with MeV protons to measure the crystal rainbow effect as well the doughnut effect [24].

Figure 2 shows a set of experimental angular patterns over a range of proton energies close to the superfocusing condition, at $\Lambda = 0.25$, which were determined on the basis of the Rainbow-Molière potential. The proton beam current

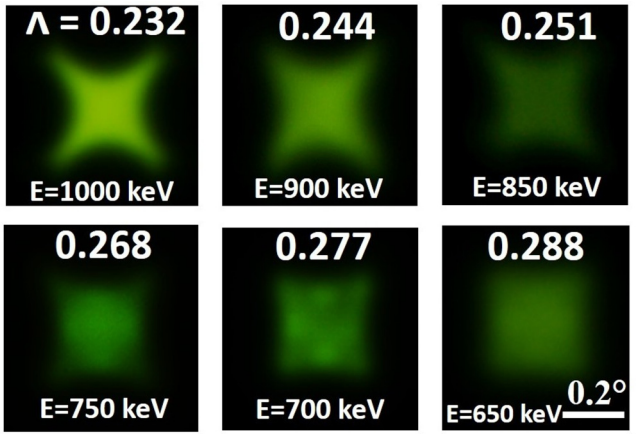

FIG. 2. Experimental axial channeling angular patterns of protons incident along the [001] axis of a 55-nm-thick Si layer for reduced crystal thicknesses from $\Lambda = 0.23$ to $\Lambda = 0.29$, shown at the top of each image. The corresponding energy E is shown at the bottom of each image, in keV.

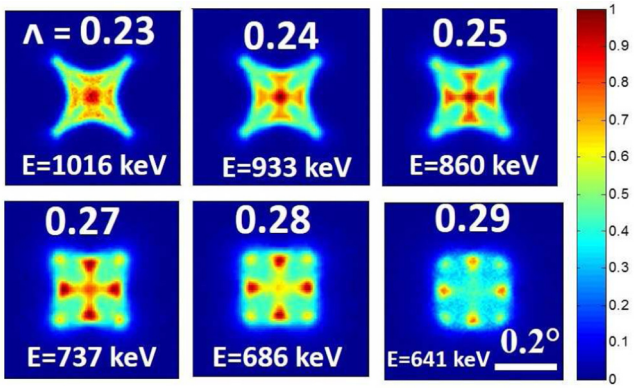

FIG. 3. FLUX simulated axial channeling patterns showing the exit angular distributions of protons incident along the [001] axis of a 55-nm-thick Si layer for reduced crystal thicknesses from $\Lambda = 0.23$ to $\Lambda = 0.29$ shown at the top of each image. The corresponding energy E is shown at the bottom of each image, in keV. Based on the Rainbow-Molière potential. Red and blue regions represent high and low intensities, respectively at each map.

and recording time for each pattern were the same to enable comparison of different angular distributions. Further experimental details can be found in Ref. [22].

The corresponding simulations of the exit angular distributions in Fig. 3 are based on the Rainbow-Molière potential close to the superfocusing condition at $\Lambda = 0.25$. For $\Lambda = 0.20$, i.e., for a proton energy well above the superfocusing energy, the simulated pattern comprises a four-point star containing no fine angular structure. At $\Lambda = 0.24$, i.e., close to the superfocusing energy, the simulated pattern changes to a square outer edge with a distinctive pattern of fine angular structure with bright dots within it. The most pronounced dot is that in the center, with four less intense dots forming a cross pattern. Four faint dots are observed in the corners of the square. Similar patterns are observed up to $\Lambda = 0.28$, with the central dot becoming fainter and the four dots forming the cross pattern becoming more intense, similar to the four dots in the corners of the square. Agreement with Fig. 2 is very good, featuring a smooth star shape at $\Lambda = 0.23$, changing to a square shape above $\Lambda = 0.25$, and forming a fine dot cross pattern at $\Lambda = 0.27$. These dots are most clearly observed at $\Lambda = 0.28$, where faint dots are also observed in the corners of the square.

Figure 4 compares the line profiles across the simulated and experimental angular patterns at proton energies of 750 and 700 keV, i.e., $\Lambda = 0.27$, 0.28, where the fine angular

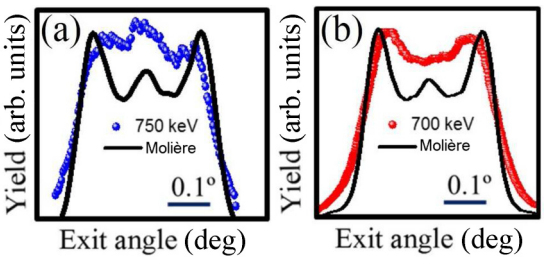

FIG. 4. Comparison of experimental line profiles at the center of angular patterns for (a) 750 and (b) 700 keV protons from simulation (Rainbow-Molière potential) in a 55-nm-thick [001] Si layer.

structure is most clearly revealed in Fig. 2. The experimental profiles were extracted across the center, both horizontally and vertically, to improve statistics. They were also normalized to the simulated profiles at the exit angle of the left maximum. For an energy of 700 keV, good agreement is found, both in terms of positions and in terms of widths of the dots forming the cross pattern. The FWHM of these fine structure dots is $\sim 0.06^\circ$, compared to the channeling critical angle for this energy, which is $\psi_c = 0.50^\circ$. Thus, we are resolving the fine structure dots with an angular width of $\sim 6\%$ of $2\psi_c$. On the other hand, the central dot for an energy of 700 keV, generated by protons emerging with very small angles, is not observed in the experimental pattern, though it is present in the simulated pattern. However, for an energy of 750 keV, the central dot is clearly seen in the experimental and simulated patterns. This is in agreement with the observation in Fig. 3, i.e., that the intensity of the central dot increases relative to the intensity of the dots forming the cross pattern when Λ decreases from 0.28 toward 0.25 and beyond. This is why the dots forming the cross pattern cannot be clearly seen in the experimental pattern for an energy of 750 keV.

The very good agreement between the experimental and simulated patterns shown in Figs. 2, 3, and 4 provides indirect evidence of the superfocusing effect and represents a measure of confidence in the FLUX simulation results, including the result given in Fig. 1(b) related to the focused proton beam width and the corresponding flux enhancement of several hundred times. Thus, while one cannot directly image this sub-Ångström-wide spatial distribution occurring due to the superfocusing effect, one may infer its existence by observing the corresponding fine structure within the angular distribution of the same beam.

In order to better understand the origin of the superfocusing effect, we further analyzed the FLUX output files; each contains a list of position and angle coordinates at the entrance and exit of the crystal for each simulated proton trajectory so the relationship between them can be found. We first examined the entrance proton positions that correspond to the fine structure bright dots in the simulated angular patterns at the exit face.

Figure 5(b) shows the simulated exit angular distribution of 860 keV protons incident on a 55-nm-thick (001) silicon layer, corresponding to the superfocusing condition. Sort areas were superposed around two different types of resolved dots, faint dots at the corners of the square (sort areas within the pink circles), and bright dots forming the cross pattern (sort areas within the black triangles). Figure 5(c) shows a potential map of the (001) silicon channel, with the potential maxima (blue areas) at the atomic strings, and at minimum (purple area) at the channel center. The entrance positions of protons from each sort area in Fig. 5(b) are superposed on the potential map in Fig. 5(c) using the same color scheme. The four bright dots forming the cross pattern are generated by protons incident between atomic strings [black dots in Fig. 5(c)], and slightly toward the channel center, where the potential gradient is directed towards the channel center. The four faint dots at the corners of the square are produced by protons incident between the atomic strings and the channel center (pink dots), where the potential gradient is also directed towards the channel center. Further analysis shows that the central dot in Fig. 5(b)

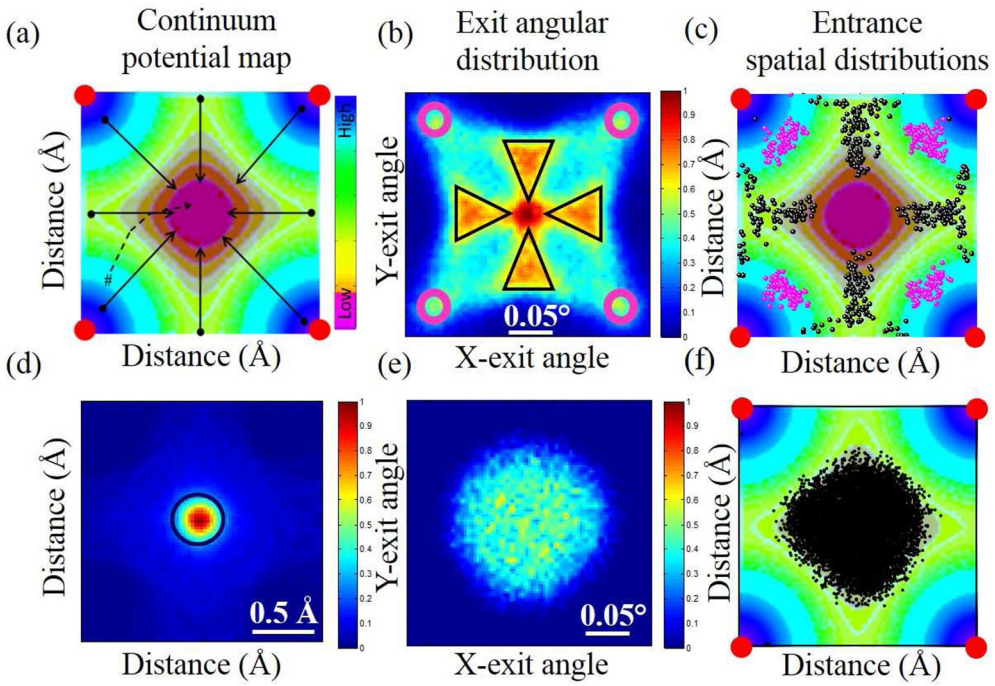

FIG. 5. (a) Continuum potential map for protons in the Si [001] unit cell, with {110} planes running horizontally and vertically. The locations of the atom strings at the corners are shown by red dots. (b) Exit angular distribution where superposed black triangles and pink circles show the sort areas used to produce the corresponding entrance position coordinate map in (c) for 0.86 MeV protons, using the same colors. (d) Exit spatial distribution for 0.86 MeV protons showing the superfocused beam at the center. A black circle shows the sort area used to produce the corresponding (e) exit angle and (f) entrance spatial distribution maps. The potential maps in (a), (c), and (f) have the same intensity scale, shown in (a).

originates from ions that are incident at the channel center and also from those directly between atomic strings, where in both cases the potential gradient is zero.

This analysis allows a simple understanding of the principle underlying the formation of resolved dots in exit angular distributions—in regions where the potential gradient is directed towards the channel center [see arrows in Fig. 5(a)], a resolved dot is formed. These beam portions oscillate back and forth across the channel with depth, with corresponding changes in exit angle resulting in the changing pattern of bright dots simulated by Krause *et al.* [17]. In other regions across the entrance channel where the potential gradient is not directed towards the center, e.g. that labelled "#" in Fig. 5(a), ions tend to spiral within the potential well at the channel center, forming a diffuse background square or circle shape within the exit angular distribution.

From this analysis, one is tempted to consider the bright dots as being important to the superfocusing effect, but the rest of Fig. 5 shows otherwise. In the lower row, we performed a similar analysis of the FLUX output position coordinates, locating a sort around the superfocused beam peak; see Fig. 5(d). We see that ions that contribute to the superfocusing peak are only those that enter close to the central potential minimum, where the potential is harmonic [Fig. 5(f)]. Figure 5(e) shows the corresponding exit angle of those ions within the superfocusing peak—they form a uniform background that is not related to the fine structure bright dots in the angular patterns. Therefore, while observation of the bright dots is important in confirming the existence of the superfocused beam condition, they originate from portions of the entrance channels that do not contribute to the superfocused beam peak.

We have used the simulated spatial and angular distributions of protons at the exit face of a thin crystal to study the superfocusing effect. We examined the minimum beam width with different potentials to define the superfocusing proton energy and then compared simulated and experimental angular distributions. This was carried out with the Rainbow-Molière potential because it provided excellent agreement between the experimental and simulated angular distributions in our previous study. While other authors have characterized the superfocusing effect at different values of Λ in simulations, we simulated the fine angular structure and combined these two facets with the experimental results to validate the superfocused proton beam width at $\Lambda = 0.25$. Resolved dots observed in experimental angular patterns represent the first, indirect experimental proof of the channeling superfocusing effect, which has the potential to be used to modify subatomic regions of the crystal, either on the surface or inside of the crystal.

The superfocusing effect is a general phenomenon that can be observed for any crystal-ion pair. A larger area within the unit cell where the potential is harmonic gives a higher flux enhancement. For instance, α-Tin has an area that is $\sim$43% greater than along the same crystallographic direction in silicon, and the simulated flux enhancement is the same factor higher. Such superfocused beams may have many applications in materials modification and analysis using MeV ions [27]

and for increasing the probability of nucleus-nucleus collision events in colliders [2]. We note that a similar channeling effect with electrons made use of a sub-Ångström beam width to map the two-dimensional molecular orbitals of silicon [28].

S.P. and N.N. acknowledge the support to this work provided by the Ministry of Education, Science and Technological Development of Serbia through project "Physics and Chemistry with Ion Beams," No. III 45006.

[1] D. S. Gemmell, Rev. Mod. Phys. **46**, 129 (1974).
[2] R. Aaij, B. Adeva, M. Adinolfi, A. Affolder, Z. Ajaltouni, S. Akar, J. Albrecht, F. Alessio, M. Alexander, S. Ali, G. Alkhazov, P. Alvarez Cartelle, A. A. Alves, Jr., S. Amato, S. Amerio, Y. Amhis, L. An, L. Anderlini, J. Anderson, R. Andreassen *et al.* (LHCb Collaboration), Phys. Rev. Lett. **114**, 132001 (2015).
[3] W. Scandale, A. Vomiero, S. Baricordi, P. Dalpiaz, M. Fiorini, V. Guidi, A. Mazzolari, G. Della Mea, R. Milan, G. Ambrosi, P. Zuccon, B. Bertucci, W. Burger, M. Duranti, G. Cavoto, R. Santacesaria, P. Valente, C. Luci, F. Iacoangeli, E. Vallazza *et al.*, Phys. Rev. Lett. **102**, 084801 (2009).
[4] N. Stojanov, S. Petrović, and N. Nešković, Nucl. Instrum. Meth. Phys. Res. Sect. B **244**, 457 (2006).
[5] Y. Demkov and J. D. Meyer, Eur. Phys. J. B **42**, 361 (2004).
[6] R. B. Alexander and R. J. Petty, Phys. Rev. B **18**, 981 (1978).
[7] R. B. Alexander, G. Dearnaley, D. V. Morgan, and J. M. Poate, Phys. Lett. A **32**, 365 (1970).
[8] N. Nešković, S. Petrović, and D. Borka, Nucl. Instrum. Methods Phys. Res. Sect. B **267**, 2616 (2009).
[9] S. Petrović, N. Nešković, V. Berec, and M. Ćosić, Phys. Rev. A **85**, 032901 (2012).
[10] P. J. M. Smulders and D. O. Boerma, Nucl. Instrum. Meth. Phys. Res. Sect. B **29**, 471 (1987).
[11] M. B. H. Breese, P. J. C. King, G. W. Grime, P. J. M. Smulders, L. E. Seiberling, and M. A. Boshart, Phys. Rev. B **53**, 8267 (1996).
[12] G. V. Dedkov, Phys. Status Solidi A **149**, 453 (1995).
[13] V. Guidi, A. Mazzolari, D. De Salvador, and L. Bacci, Phys. Rev. Lett. **108**, 014801 (2012).
[14] D. N. Wijesundera, K. B. Ma, X. Wang, B. P. Tilakaratne, L. Shao, and W.-K. Chu, Phys. Lett. A **376**, 1763 (2012).
[15] L. J. M. Selen, L. J. van Ijzendoorn, P. J. M. Smulders, and M. J. A. de Voigt, Nucl. Instrum. Meth. Phys. Res. Sect. B **190**, 570 (2002).
[16] S. Petrović, N. Nešković, M. Ćosić, M. Motapothula, and M. Breese, Nucl. Instrum. Meth. Phys. Res. Sect. B **360**, 23 (2015).
[17] H. F. Krause, J. H. Barrett, S. Datz, P. F. Dittner, N. L. Jones, J. Gomez del Campo, and C. R. Vane, Phys. Rev. A **49**, 283 (1994).
[18] H. F. Krause, S. Datz, P. F. Dittner, J. Gomez del Campo, P. D. Miller, C. D. Moak, N. Nešković, and P. L. Pepmiller, Phys. Rev. B **33**, 6036 (1986).
[19] L. C. Feldman, J. W. Mayer, and S. T. Picraux, *Materials Analysis by Ion Channeling* (Academic Press, New York, 1982).
[20] M. R. Altman, L. C. Feldman, and W. M. Gibson, Phys. Rev. Lett. **24**, 464 (1970).
[21] N. Nešković and B. Perović, Phys. Rev. Lett. **59**, 308 (1987).
[22] S. Petrović, L. Miletić, and N. Nešković, Phys. Rev. B **61**, 184 (2000).
[23] Z. Y. Dang, M. Motapothula, Y. S. Ow, T. Venkatesan, M. B. H. Breese, M. A. Rana, and A. Osman, Appl. Phys. Lett. **99**, 223105 (2011).
[24] M. Motapothula, S. Petrović, N. Nešković, Z. Y. Dang, M. B. H. Breese, M. A. Rana, and A. Osman, Phys. Rev. B **86**, 205426 (2012).
[25] M. Motapothula, Z. Dang, T. Venkatesan, M. Breese, M. Rana, and A. Osman, Phys. Rev. Lett. **108**, 195502 (2012).
[26] M. Motapothula, Z. Y. Dang, T. Venkatesan, M. B. H. Breese, M. A. Rana, and A. Osman, Nucl. Instrum. Meth. Phys. Res. Sect. B **283**, 29 (2012).
[27] I. Stensgaard and F. Jakobsen, Phys. Rev. Lett. **54**, 711 (1985).
[28] R. Hovden, H. L. Xin, and D. A. Muller, Phys. Rev. B **86**, 195415 (2012).